Study of self-generated fields in strongly-shocked, low-density systems using broadband proton radiography

R. Hua, H. Sio, S. C. Wilks, F. N. Beg, C. McGuffey, M. Bailly-Grandvaux, G. W. Collins, and Y. Ping

Study of self-generated fields in strongly-shocked, low-density systems using broadband proton radiography

R. Hua,[1] H. Sio,[2] S. C. Wilks,[3] F. N. Beg,[1] C. McGuffey,[1] M. Bailly-Grandvaux,[1] G. W. Collins,[3] and Y. Ping[3]

[1]*Center for Energy Research, University of California, San Diego, La Jolla, California 92093, USA*
[2]*Plasma Science and Fusion Center, Massachusetts Institute of Technology, Cambridge, Massachusetts 02139, USA*
[3]*Lawrence Livermore National Lab, 7000 East Avenue, Livermore, California 94550, USA*

We report results from experiments on the study of field generation at the shock front in low-density gas configured in quasi-planar geometry using broad-energy proton probing. Experiments were conducted using three long pulse laser beams with a total energy of 6.4 kJ in 2 ns for shock generation and an 850 J, 10 ps short pulse laser to produce broadband protons for radiography. Observations of the deflection pattern of probe protons show the existence of self-generated electric fields at the shock front with the electric potential on the order of 300 V. Analytical and particle tracking methods support this conclusion. *Published by AIP Publishing.*
[http://dx.doi.org/10.1063/1.4995226]

Radiation hydrodynamic codes are frequently used to predict the evolution of plasmas in inertial confinement fusion (ICF) by modeling a single average-ion species fluid and an electron fluid. However, there are discrepancies between experimental data and these codes' predictions. For example, an anomalously low shock yield has been reported in various implosion experiments using targets with multiple fuel species, such as Deuterium-Tritium[1] and Deuterium-³Helium.[2] In ICF, high velocity shocks converge to the center of a low-density gas, resulting in a dramatic increase in the ion temperature and the ion-ion collision mean free path. The ion-ion collision mean free path can become comparable to the target radius during the shock rebound. In the case where the Knudsen number (the ratio of ion mean free path to minimum shell radius) is near unity, the kinetic theory is more appropriate than hydrodynamics to explain the underlying physics.[3,4] Experimentally, ion thermal decoupling has been observed;[2] this phenomenon associated with kinetic effects could potentially contribute to the anomalies mentioned above.

Self-generation of electric fields at the plasma shock front is another kinetic effect that could affect the shock convergence phase.[5–7] Several candidate mechanisms explaining the formation of these fields were first proposed by Amendt *et al.*,[8] and ion-kinetic simulation work was later performed by Bellei *et al.*[9] These fields, which are generated on the basis of charge separation,[10,11] are present at the fronts of strong plasma shocks, where large electron pressure gradients exist.[12,13] Electrons, being more mobile than ions, are pushed slightly ahead of the shock, producing a negative charge surplus in the front of the shock. This creates an electric field pointing along the shock propagation direction.

Direct observations of the field were made by Rygg *et al.*[14] and Li *et al.*[15] in implosion experiments using mono-energetic proton radiography. However, limited by the spherical geometry, detection of the inward propagating shock fronts and the associated electric fields could not be distinguished from the ablator encompassing them by proton radiography. In addition, it is difficult to accurately constrain the field strength using the single energy datum provided by mono-energetic protons.

In this letter, we present results from a recently developed platform[16] using planar geometry and broadband proton radiography to investigate the shock front on the OMEGA-EP laser.[17,18] Data from multiple proton energies are collected for each shot, which enabled the discrimination of the ablator and the shock front as well as quantitative constraining of the field strength. An electric field on the order of a few microns wide and 300 V potential at the front of a 0.5 Mbar, Mach 10 shock is reported.

A schematic diagram of the experimental setup is illustrated in Fig. 1(a). The main target was a cylindrical tube of 2 mm diameter and 5 mm length. The tube had 50 μm Kapton walls and two 1 μm thick Kapton windows along the line-of-sight of proton trajectories towards the radiochromic film (RCF) stack.[19] Pure helium gas filled the gas tube through the filling tube, which is at the right end of the gas tube in green and purple. A strong shock was created in the gas by laser ablation of a polystyrene (CH) foil located on the left end of the gas tube. Three synchronized long pulse laser beams were used to drive the shock by delivering a total energy of 6.4 kJ in a 2 ns square pulse. A plastic cone was mounted around the CH foil on the left of the gas tube for plasma debris shielding. A semicircular copper grid with 55 μm wires and 340 μm period was attached to the bottom of the tube as a spatial reference.

The proton imaging scheme is composed of a back-lighter target and the RCF stack, respectively located at 7.5 mm and 12 cm on either side of the tube, corresponding to a magnification of 17$\times$ for the radiography. The proton backlighter consisted of a 40 μm copper foil strip protected by a plastic sleeve and a front foil. The front foil was 5 μm copper and separated from the copper foil strip by 1 mm to shield it from the target plasma. The Cu strip was illuminated by a short pulse laser with 850 J in 10 ps. A proton beam with energy
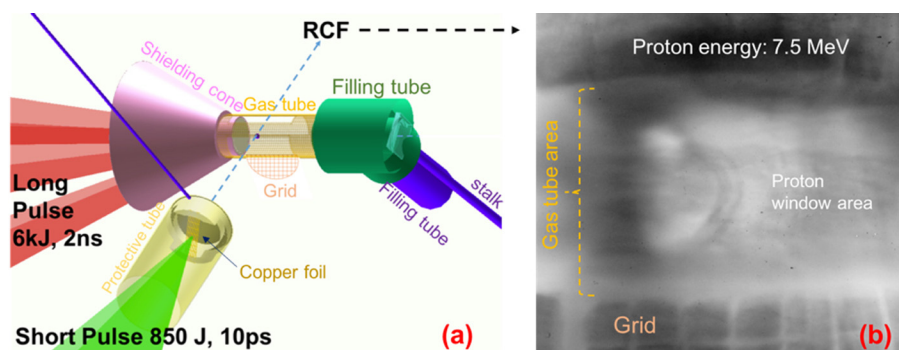
FIG. 1. (a) Schematic of the experimental setup. (b) A typical proton radiograph taken with 7.5 MeV protons at 4 ns after the start of the long pulse. The gas-cell target was filled with 3 atm helium and driven by three lasers with 6.4 kJ over 2 ns.

spanning 20 MeV was generated from the target normal sheath acceleration mechanism.[20]

The film stack had a 100 μm aluminum filter in the front, followed by 20 layers of GAFChromic HD-V2 films and then 8 layers of GAFChromic MD-V3 films.[21,22] Each film is most sensitive to a specific energy band of 1–2 MeV. Thus, the entire stack can produce up to 28 radiograph frames using protons spanning 3 MeV to 22 MeV.

A typical radiograph taken by 7.5 MeV protons 4 ns after the start of the laser drive is shown in Fig. 1(b). The fill gas was pure helium at 3 atm (corresponding to an initial density of 0.5 mg/cm^3). Two dark rings are detected inside the window area, which are shown on a larger scale and with a higher contrast in Fig. 2. In the figure, a 2D space map of the proton signal is plotted on the grayscale, and a lineout along the center of the shock is plotted in red. The spatial scale of Fig. 2 is adjusted to the objective plane by dividing the measurements on the film by the magnification of 17.

The origins of the two rings are identified to be the density scattering effect from the gas-ablator interface and field deflection at the shock front using the 2-D radiation hydrodynamic code FLASH.[23] Figure 3(a) shows simulation results including profiles along the shock propagation direction for density (blue) and the electron pressure (green). Experimentally, the shock traveling distance at 4 ns is around 1.2 mm from the radiography measurement, which is in good agreement with the shock front position in the simulation as shown in Fig. 3(a). The two rings' spacing is measured to be around

140 μm accounting for the magnification of the radiograph, which is reasonably close to the separation between the shock front and the gas-ablator interface predicted by simulation (160 μm) as in Fig. 3(a). Therefore, we attribute the two rings to correspond to the shock front and the gas-ablator interface. In addition to the data point at 4 ns, a data point from a nominally identical shot with proton probing at 3 ns is also included in comparison with the simulation as shown in Fig. 3(b). At 3 ns, only one ring is observed by the radiography, whose position is plotted in black. It is likely that the shock front is not sufficiently separated from the ablator such that it cannot be resolved by the proton radiography at that time. The simulated distances of the ablator gas interface and the shock front are plotted vs time in solid blue and dashed green lines, respectively. The experimental data are displayed by circles with error-bars. The shock breakout from the ablator at an early time and its propagation away from the ablator at a later time are well depicted in Fig. 3(b). Overall, the FLASH simulation is in agreement with all three data points within the error bars, confirming our identification of the two rings.

We here discuss the calculation of the density scattering by the simulated ablator gas interface using Highland's formula.[24] In this calculation, the target density is 0.1 g/cm^3 as in simulation and the target thickness is ~1 mm (radius of the tube cross-section). Using the calculated scattering angle, a proton ring of ~70 μm wide is expected on the radiography film, which shows good agreement with the measurement of the inner ring's width. This gives us additional confidence that the FLASH simulation is reasonable in reproducing our experimental conditions. Therefore, outputs such as pressure and temperature are used in the analyses described below.

Not all layers in the RCF stack record deflection ring features that can be used for measurements, limited by the field potential as well as the image quality. The front-most layers collect signals from low energy protons. The deepest layers, collecting protons with up to 22 MeV, did not show a detectable ring with good contrast to the background presumably because these high energy particles were less susceptible to the fields. This phenomenon is also observed using a ray-tracing program for proton imaging that will be discussed later.

As there is a density gradient at the shock front, density scattering can also be a factor for the outer ring generation. To figure out this possibility, we estimate the scattering angle by the density gradient at the shock front using the Highland formula again. The densities on the leading and trailing sides
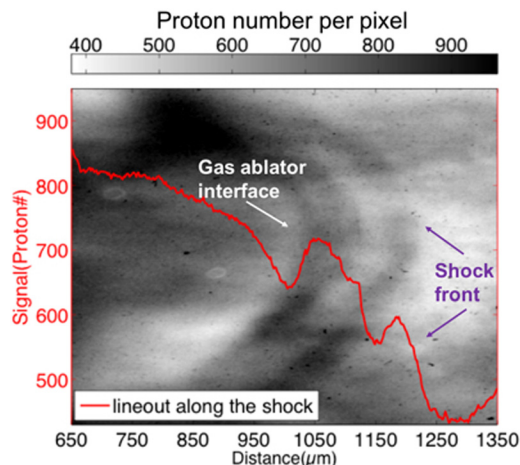

FIG. 2. Shock front area captured by 7.5 MeV protons at 4 ns. A lineout across the center of the shock is plotted in red. The x-axis represents the distance from the initial ablator position. The spatial scale is adjusted to the objective plane by dividing the film measurements by the magnification of 17.
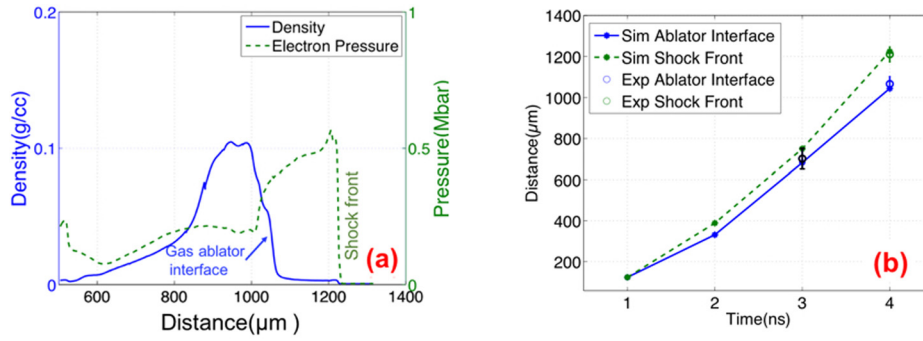
FIG. 3. (a) FLASH simulation result for the shot shown in Fig. 2, which was filled with 3 atm and driven by a laser with 6.4 kJ in 2 ns. The x-axis represents the distance from the initial ablator position (zero point), where the shock was initiated. The snapshot was taken at 4 ns. The density profile across the shock center is plotted in solid blue, and the electron pressure is shown by a dashed green line. The pressure at the shock front is ∼0.5 Mbar. (b) Simulated shock front (dashed green curve) and ablator-gas interface (blue curve) movement as a function of time. The circles with error-bars correspond to the data. Only one ring is observed at 3 ns, which could be the combination of both the interface and the shock front, and is plotted in black.

of the shock front are 3.3 mg/cm^3 and 0.5 mg/cm^3 (compression is about 6–7× for a single shock with the radiation effect taken into account), respectively; the scattering effect is only able to make a ring up to 1 μm wide on the film for protons with energies between 5 and 8 MeV. Compared to the measurements of ∼50 μm, density scattering is negligible at the shock front.

Now, we will discuss the process used to extract the E field information, which is obtained by analyzing the outer ring observed in the radiographs. This ring is observed with the decreasing width for increasing proton energy because slower protons are more deflected by the field. The analytical solution of the proton deflection angle due to a radial electric field at a spherical surface was studied by Kugland *et al.*[25] The process is described as follows: the deflecting component of a proton traveling in the Z-direction through a field transversely can be described by the following equation

$$\frac{dv_x}{dt} = -\frac{e}{m_p}\frac{\partial \phi}{\partial x}, \tag{1}$$

where x is along the field pointing direction, v_x is the deflecting component caused by the field, m_p is the proton mass, e is the electric charge, and ϕ is the electric potential. Based on the relation that $dz = v_z dt$, the deflection angle then can be expressed as

$$\alpha_x = \frac{v_x}{v_z} = -\frac{e}{2E_p}\frac{\partial}{\partial x}\int \phi(x,y,z)dz \tag{2}$$

Transforming the equation into spherical coordinates and assuming that the field profile is a delta function right at a spherical surface (a valid assumption when the field width is significantly smaller than the radius) give the deflection angle

$$\alpha = -\frac{4er}{E_p}\int \frac{dr}{\sqrt{R^2 - r^2}}\frac{d\phi}{dr} = \frac{4e\phi}{E_p}\frac{R}{\sqrt{2R\Delta x}}, \tag{3}$$

in which R is the spherical radius and Δx is the proton displacement along the deflecting direction in the field. R is ∼935 μm by the measurement, and Δx is assumed to be on the scale of the ion ion mean free path at the shock front, ∼0.4 μm.[12] The ring width is determined by the spread

between the protons experiencing no deflection ($\alpha = 0$ when a proton passed by the sphere) and those experiencing maximum deflection by the field. Therefore, the potential is calculated using the measured ring widths and their corresponding proton energies as shown in Fig. 4. The FWHM (full width half maximum) of the rings is measured from the lineouts from three layers in between 5 MeV and 8 MeV. One example of the lineouts is the shown as the red curve in Fig. 2. Data points are plotted as blue circles, from which the electric potential is estimated to be 320–350 V within the measurement errors. The black dashed line shows the expected behavior using the above equation when potential equals 330 V.

In addition to these calculations, a ray tracing program to model the proton trajectories in the presence of electric fields is used to reproduce the images recorded by the film. In this process, a hemisphere shell-shaped electric field pointing outwards is implemented with a potential of 330 V. The field is uniformly distributed, and the radius of the sphere is 935 μm. The proton source size is taken to be 10 μm.[26] The output image has been adjusted such that the resolution is about the same as the data. Two simulated images by protons of 5.8 MeV (a) and 12.3 MeV (b) are displayed in Fig. 5. As expected, the results show a strong energy dependence. In the simulated images, widths are also
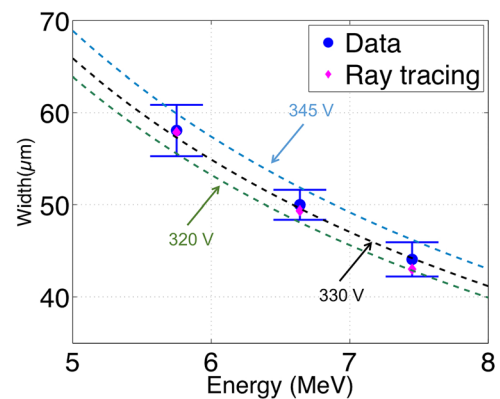

FIG. 4. Ring width versus probing proton energies. The dark blue dots with error-bars are experimental data, and the pink dots are results from a ray tracing program. The three dashed curves are from Eq. (3), which show the result for potentials of 320 V, 330 V, and 345 V.
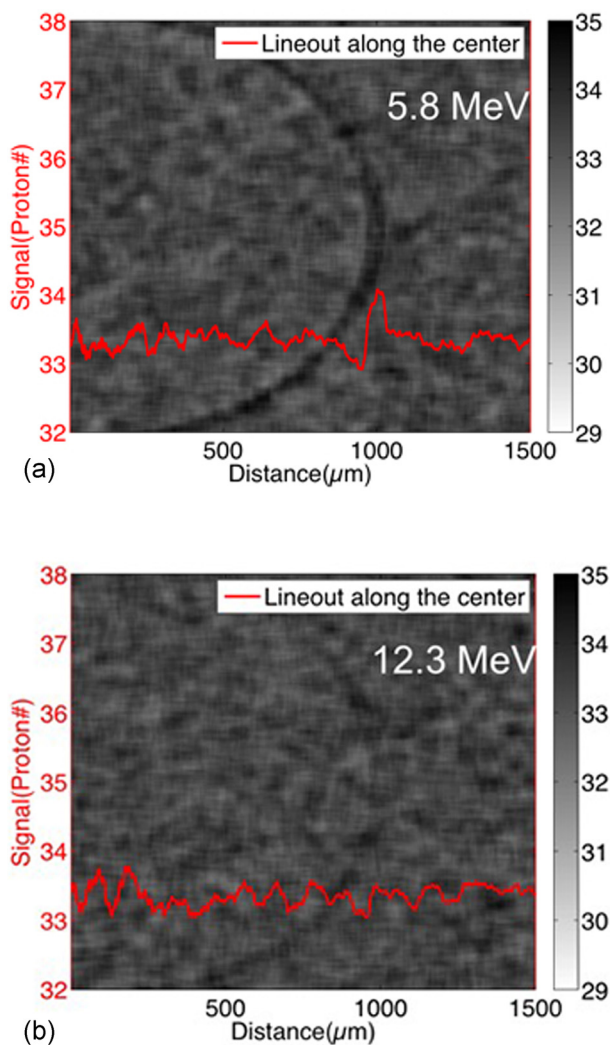
FIG. 5. Proton images by the ray tracing program at two energies, 5.8 MeV (a) and 12.3 MeV (b). The electric field was set up to be 330 V, and the energy dependence is seen.

measured at the same three proton energies as shown in Fig. 4 and are plotted in pink dots.

Now, we discuss the reasons for these fields. A couple of candidate mechanisms have been proposed to explain the field existence since its observation.[15] One such mechanism is attributed to the gradient in electron pressure, which can give rise to an electric field. In this case, free electrons can be pushed slightly ahead of ions due to their higher mobility, thus creating the electric field pointing along the shock. The field strength can be expressed as $E = -\nabla P/en$, where n is the electron density, P is the electron pressure, and e is the electric charge. With the pressure profile shown in Fig. 3(a), the electric potential created at the shock front is ~600 V.

The second approach compares the potential with the thermal energy.[27] In this mechanism, the electrons, being more mobile than ions, will diffuse ahead of the shocked ions due to the density gradient existing at a shock front, thus giving rise to an electric field. The potential formed in this process is mostly dependent on the electron temperature as expressed by $\Delta\Phi \approx yk_BT_e/e \cdot \ln(\rho_2/\rho_1)$, a simple expression that electrons can go no further than when they have lost all their thermal energy in overcoming the field potential. Here, ρ_1 and ρ_2 are the densities of shocked and

un-shocked materials. As the electron temperature is around 300 eV and the compression is around $6\times$–$7\times$, the field potential is about 600 V predicted by this model.

These theoretical considerations predict a higher electric potential compared to the experimental data. There are a couple of possibilities for this difference; first, the FLASH simulations were conducted in 2D, which might contribute to a sharper jump at the shock front when compared to the experiment. Further, in the analytical equation, the proton displacement in the field is considered to be 0.4 μm according to the ion mean free path calculation, which might have underestimated the potential since in reality the displacement could possibly be longer than the mean free path.

In summary, a strong self-generated electric field at a 0.5 Mbar shock front created in a low density system has been both experimentally observed using broad band proton radiography and theoretically predicted to be on the same scale. Additionally, 2-D radiation hydrosimulations have been conducted, and the E field inferred from them also is favorably comparable with the experimental results. Possible reasons as to why the results are not an exact match are presented.

[1]H. W. Herrmann, J. R. Langenbrunner, J. M. Mack, J. H. Cooley, D. C. Wilson, S. C. Evans, T. J. Sedillo, G. A. Kyrala, S. E. Caldwell, and C. S. Young, Phys. Plasmas **16**, 056312 (2009).
[2]H. G. Rinderknecht, M. J. Rosenberg, C. K. Li, N. M. Hoffman, G. Kagan, A. B. Zylstra, H. Sio, J. A. Frenje, M. Gatu Johnson, and F. H. Séguin, Phys. Rev. Lett. **114**, 025001 (2015).
[3]M. J. Rosenberg, H. G. Rinderknecht, N. M. Hoffman, P. A. Amendt, S. Atzeni, A. B. Zylstra, C. K. Li, F. H. Séguin, H. Sio, and M. Gatu Johnson, Phys. Rev. Lett. **112**, 185001 (2014).
[4]K. Molvig, N. M. Hoffman, B. J. Albright, E. M. Nelson, and R. B. Webster, Phys. Rev. Lett. **109**, 095001 (2012).
[5]M. Casanova, O. Larroche, and J.-P. Matte, Phys. Rev. Lett. **67**, 2143 (1991).
[6]A. L. Velikovich, K. G. Whitney, and J. W. Thornhill, Phys. Plasmas **8**(10), 4524 (2001).
[7]I. R. Smirnovskii, Plasma Phys. Rep. **26**, 225 (2000).
[8]P. A. Amendt, J. L. Milovich, S. C. Wilks, C. K. Li, R. D. Petrasso, and F. H. Séguin, Plasma Phys. Controlled Fusion **51**, 124048 (2009).
[9]C. Bellei, P. A. Amendt, S. C. Wilks, M. G. Haines, D. T. Casey, C. K. Li, R. Petrasso, and D. R. Welch, Phys. Plasmas **20**, 012701 (2013).
[10]P. Amendt, O. L. Landen, H. F. Robey, C. K. Li, and R. D. Petrasso, Phys. Rev. Lett. **105**, 115005 (2010).
[11]G. Kagan and X.-Z. Tang, Phys. Plasmas **19**, 082709 (2012).
[12]M. Y. Jaffrin and R. F. Probstein, Phys. Fluids **7**, 1658 (1964).
[13]D. T. Casey, J. A. Frenje, M. Gatu Johnson, M. J.-E. Manuel, H. G. Rinderknecht, N. Sinenian, F. H. Séguin, C. K. Li, R. D. Petrasso, and P. B. Radha, Phys. Rev. Lett. **108**, 075002 (2012).

14 J. R. Rygg, F. H. Séguin, C. K. Li, J. A. Frenje, M. J.-E. Manuel, R. D. Petrasso, R. Betti, J. A. Delettrez, O. V. Gotchev, and J. P. Knauer, Science **319**, 1223 (2008).

15 C. K. Li, F. H. Séguin, J. R. Rygg, J. A. Frenje, M. Manuel, R. D. Petrasso, R. Betti, J. Delettrez, J. P. Knauer, and F. Marshall, Phys. Rev. Lett. **100**, 225001 (2008).

16 H. Sio, R. Hua, Y. Ping, C. McGuffey, F. Beg, R. Heeter, C. K. Li, R. D. Petrasso, and G. W. Collins, Rev. Sci. Instrum. **88**, 013503 (2017).

17 L. J. Waxer, D. N. Maywar, J. H. Kelly, T. J. Kessler, B. E. Kruschwitz, S. J. Loucks, R. L. McCrory, D. D. Meyerhofer, S. F. B. Morse, and C. Stoeckl, Opt. Photonics News **16**, 30 (2005).

18 C. Stoeckl, J. A. Delettrez, J. H. Kelly, T. J. Kessler, B. E. Kruschwitz, S. J. Loucks, R. L. McCrory, D. D. Meyerhofer, D. N. Maywar, S. F. B. Morse, J. Myatt, A. L. Rigatti, L. J. Waxer, J. D. Zuegel, and R. B. Stephens, Fusion Sci. Technol. **49**, 367 (2006), available at http://www.tandfonline.com/doi/abs/10.13182/FST06-A1155.

19 M. Borghesi, A. Schiavi, D. H. Campbell, M. G. Haines, O. Willi, A. J. MacKinnon, L. A. Gizzi, M. Galimberti, R. J. Clarke, and H. Ruhl, Plasma Phys. Controlled Fusion **43**, A267 (2001).

20 S. C. Wilks, A. B. Langdon, T. E. Cowan, M. Roth, M. Singh, S. Hatchett, M. H. Key, D. Pennington, A. MacKinnon, and R. A. Snavely, Phys. Plasmas **8**, 542 (2001).

21 A. Mack, G. Mack, D. Weltz, S. G. Scheib, H. D. Böttcher, and V. Seifert, Med. Phys. **30**, 2399 (2003).

22 A. B. Zylstra, C. K. Li, H. G. Rinderknecht, F. H. Séguin, R. D. Petrasso, C. Stoeckl, D. D. Meyerhofer, P. Nilson, T. C. Sangster, and S. Le Pape, Rev. Sci. Instrum. **83**, 013511 (2012).

23 B. Fryxell, K. Olson, P. Ricker, F. X. Timmes, M. Zingale, D. Q. Lamb, P. MacNeice, R. Rosner, J. W. Truran, and H. Tufo, Astrophys. J. Suppl. Ser. **131**, 273 (2000).

24 V. L. Highland, Nucl. Instrum. Methods **129**, 497 (1975).

25 N. L. Kugland, D. D. Ryutov, C. Plechaty, J. S. Ross, and H. S. Park, Rev. Sci. Instrum. **83**, 101301 (2012).

26 A. Macchi, M. Borghesi, and M. Passoni, Rev. Mod. Phys. **85**, 751 (2013).

27 Y. B. Zel'dovich and Y. P. Raizer, *Physics of Shock Waves and High-Temperature Hydrodynamic Phenomena* (Dover Publications, 2012), p. 522.